


Measuring and imaging nanomechanical motion with laser light

Andreas Barg¹ · Yeghishe Tsaturyan¹ · Erik Belhage¹ · William H. P. Nielsen¹ ·
Christoffer B. Møller¹ · Albert Schliesser¹ 

Received: 2 September 2016 / Accepted: 7 November 2016 / Published online: 15 December 2016
© Springer-Verlag Berlin Heidelberg 2016

Abstract We discuss several techniques based on laser-driven interferometers and cavities to measure nanomechanical motion. With increasing complexity, they achieve sensitivities reaching from thermal displacement amplitudes, typically at the picometer scale, all the way to the quantum regime, in which radiation pressure induces motion correlated with the quantum fluctuations of the probing light. We show that an imaging modality is readily provided by scanning laser interferometry, reaching a sensitivity on the order of $10 \text{ fm/Hz}^{1/2}$, and a transverse resolution down to $2 \mu\text{m}$. We compare this approach with a less versatile, but faster (single-shot) dark-field imaging technique.

Electronic supplementary material The online version of this article (doi:[10.1007/s00340-016-6585-7](https://doi.org/10.1007/s00340-016-6585-7)) contains supplementary material, which is available to authorized users.

This article is part of the topical collection “Enlightening the World with the Laser” - Honoring T. W. Hänsch guest edited by Tilman Esslinger, Nathalie Picqué, and Thomas Udem.

This article is dedicated to Theodor W. Hänsch on the occasion of his 75th birthday. Fortunate enough to have several chances to work with him, I could learn about his unique approach to experimental science. The first bit came right during my interview for a PhD position: When somebody claimed that all simple interesting things had already been done, he insisted that great experiments do not have to be complicated—if they are *clever*. It felt wise already then, now I know (better) how true it is. And I’m looking forward to seeing more clever experiments emerge from the Munich laboratories. Happy Birthday!

✉ Albert Schliesser
albert.schliesser@nbi.dk

¹ Niels Bohr Institute, Blegdamsvej 17, 2100 Copenhagen, Denmark

1 Introduction

Lasers are indispensable tools in science and technology today. They heal eyes, power the Internet, and print objects in 3D. They have also revolutionized atomic physics: Techniques such as laser cooling and optical frequency metrology have enabled the creation of new states of matter, precision tests of fundamental physical laws, and the construction of clocks more accurate than ever before. The lasers’ key feature—high spatial and temporal coherence of the emitted light—is a unique asset, too, for the measurement of distance and motion. The laser interferometric gravitational wave observatory (LIGO) has provided the most recent, spectacular demonstration of this fact, with the direct detection of gravity waves [1].

While LIGO is concerned with the apparent displacement of kg-scale test masses, laser-based techniques are also an excellent choice to track the motion of micro- and nanoscale objects. Indeed, lasers have been used to measure a micro-cantilever’s motion induced by the magnetic force of a single electron spin [2], providing only one example of the force and mass sensing capabilities of laser-transduced mechanical devices. The interaction of laser light and nanomechanical motion, which lies at the heart of any such measurement scheme, has, itself, moved to the center of attention recently. Research in the field of cavity optomechanics [3] explores the fundamental mechanisms—governed by the laws of quantum mechanics, of course—and the limitations and opportunities for mechanical measurements that they imply. Without even making an attempt at a comprehensive review of the vast activity in this field, we illustrate recent progress through a selection of our own results below.

For this research, it is often crucial to understand not only the spectral properties of the mechanical resonators, such as their eigenmodes’ frequency and lifetime, but also

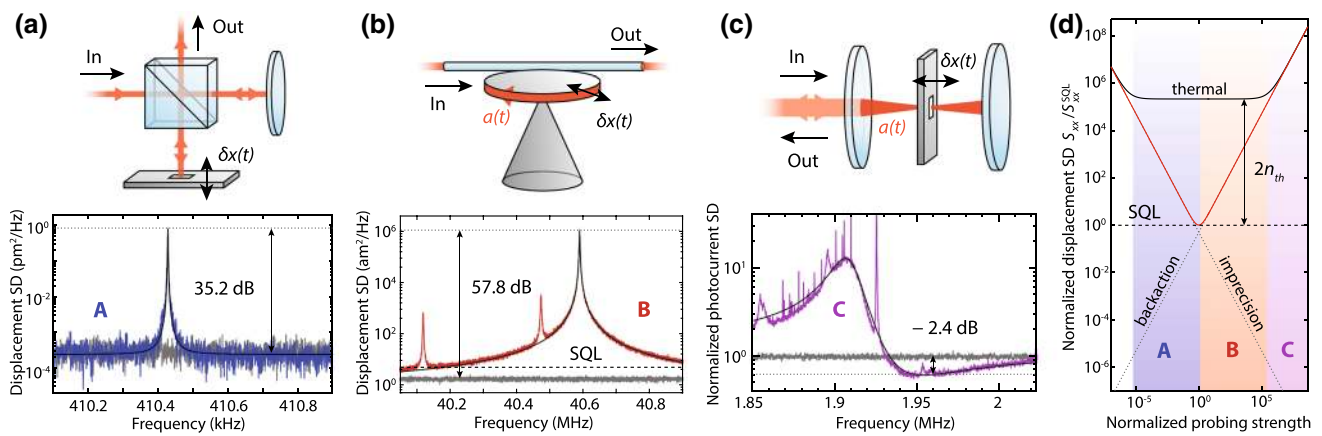


Fig. 1 Probing mechanical motion $\delta x(t)$ by laser interferometry. **a** Simple two-path interferometer, involving reflection off the mechanical device (top). The thermal motion (blue trace) of a high- Q membrane is readily resolved above the measurement imprecision background (gray). **b** Cavity-enhanced measurement, here of a radial-breathing mode of an optical whispering-gallery-mode resonator (top). Thermal motion (red trace) is far above the imprecision background (gray), which is itself below the resonant standard quantum limit (SQL) for this mechanical mode (from [10]). **c** Cavity-based

measurements of highly coherent mechanical resonators, here a high- Q silicon nitride membrane placed inside a Fabry–Perot resonator (top). Quantum backaction starts to dominate over the thermal motion of the device, inducing correlations that lead to squeezing of the output light (violet trace) below the vacuum noise (gray), among others (from [20]). **d** Comparison of the relative levels of measurement imprecision, backaction, and thermomechanical noise in the measurement regimes depicted in the examples (a)–(c)

the modes’ spatial displacement patterns, as it determines the effective mass m_{eff} , and therefore the optomechanical interaction strength. The pattern can also strongly affect the modes’ coherence properties. Both are particularly important for the development of new resonator systems. For example, the full knowledge of the mode shape has allowed us to design resonators with a “soft” phononic crystal clamping that enables unprecedented room-temperature quality factors $Q > 10^8$ at MHz frequencies [4]. While finite-element simulations of mechanical modes become ever more powerful and accurate, they often miss fabrication imperfections and substrate effects that can lead to broken symmetries or mode hybridization, among others. For this reason, we have developed several laser-based imaging techniques of micro- and nanomechanical devices. In this article, we provide a description of these highly useful tools.

2 Laser interferometry and spectroscopy

A simple two-path interferometer (Fig. 1a) constitutes the most straightforward approach to measuring mechanical displacements. One arm’s path involves the reflection off the mechanical device’s surface, so that its motion modulates the path length difference between the two arms. If the interferometer is biased to the optimum point, it can detect displacement (double-sided) spectral densities S_{xx} down to a level of [5]

$$S_{xx}^{1/2} = \frac{\lambda}{2\pi} \frac{1}{\sqrt{\eta_d P / \hbar \omega}} \tag{1}$$

It is limited by the quantum phase uncertainty of the coherent state that the laser emits, referred to as the measurement imprecision. Here, λ , ω , and P are the wavelength, angular frequency, and power of the employed laser light, respectively. η_d is the detection efficiency, which also absorbs penalties in the sensitivity due to optical losses, insufficient interference contrast, etc. Equation (1) implies that within a bandwidth BW, the smallest displacements that can be recovered with unity signal-to-noise ratio are given by $\delta x_{\text{min}} / \sqrt{\text{BW}} = \sqrt{S_{xx}}$.

Our instrument (detailed below) employs a near-infrared laser and mW-scale probing powers and typically achieves a $S_{xx}^{1/2} \sim 10 \text{ fm} / \sqrt{\text{Hz}}$ displacement sensitivity, consistent with Eq. (1). This compares favorably with the picometer-scale thermal root-mean-square (RMS) displacement $\delta x_{\text{th}} = \sqrt{k_B T / m_{\text{eff}} \Omega_m^2}$ of the mechanical resonators we employ [4, 6], with nanogram mass m_{eff} and MHz frequency $\Omega_m / 2\pi$ at room temperature T . In the Fourier domain, the spectral density of the thermal motion is spread over the mechanical linewidth $\Gamma_m = \Omega_m / Q$. Correspondingly, a nearly four-order-of-magnitude signal-to-noise ratio $S_{xx}^{\text{th}}(\Omega_m) / S_{xx}$ between the peak thermal displacement spectral density $S_{xx}^{\text{th}}(\Omega_m) = \frac{\delta x_{\text{th}}^2}{\Gamma_m / 2}$ and the noise background S_{xx} can be reached already with quality factors in the millions. An example for such a measurement is shown in Fig. 1a.

This sensitivity is insufficient, however, for the detection of displacements at the level of the mechanical RMS zero-point fluctuations $\delta x_{\text{zpf}} = \sqrt{\hbar / 2 m_{\text{eff}} \Omega_m}$, which are at the femtometer level for the parameters discussed above.

An optical cavity is needed to enhance the interaction between light and motion, recycling the light for a number of roundtrips that is commensurate with the finesse \mathcal{F} of the cavity. The phase shift of the light emerging from the cavity is multiplied correspondingly, allowing more sensitive detection with the same amount of laser light. In the simplest case of resonant probing ($\omega = \omega_c$, the cavity resonance frequency), the quantum imprecision noise is equivalent to displacement spectral densities of [7]

$$S_{xx}^{1/2}(\Omega) = \frac{\lambda}{16\eta_c \mathcal{F}} \frac{1}{\sqrt{\eta_d P / \hbar \omega}} \sqrt{1 + \left(\frac{\Omega}{\kappa/2}\right)^2}, \quad (2)$$

for a Fabry–Perot resonator with a moving end mirror (in the case of a whispering-gallery-mode resonator whose radius is measured, $\lambda \rightarrow \lambda/\pi$). Note that the sensitivity now acquires a dependence on the Fourier frequency Ω , here a simple cutoff behavior for frequencies larger than the cavity half linewidth $\kappa/2$, as well as the degree of cavity overcoupling η_c .

Figure 1b shows an example of such a measurement, in this case performed on the radial-breathing mode of a silica whispering-gallery-mode resonator [7], with the help of a polarization spectroscopy technique [8]. It resolves not only thermal motion with a large signal-to-noise ratio (here, about 58 dB), but also achieves an imprecision noise below that at the resonant standard quantum limit (SQL), $S_{xx}^{SQL}(\Omega_m) = \frac{\delta x_{zpf}^2}{\Gamma_m/2}$. Note that this coincides with the peak spectral density of ground-state fluctuations [9], for this device with $\Omega_m/2\pi = 40.6$ MHz, $\Gamma_m = 1.3$ kHz and $m_{\text{eff}} = 10$ ng at the level of $S_{xx}^{SQL}(\Omega_m) = (2.2 \text{ am})^2/\text{Hz}$ [10].

Cavity-enhanced laser interferometry has also been applied to nanomechanical resonators all the way down to the molecular scale. For example, it was shown that a fiber-based optical microcavity can resolve the thermal motion of carbon nanotubes [11]. Another successful sensing scheme consists in introducing nanomechanical resonators in the near field of optical whispering-gallery-mode resonators. It achieves imprecision well below that at the SQL of stressed silicon nitride nanostrings with picogram masses and $Q \sim 10^6$ [12–14]. It is also expected that optical cavities suppress diffraction losses through preferential scattering into the cavity mode.

To track or steer coherent dynamics of mechanical resonators at the level of their vacuum fluctuations, yet higher sensitivities are required [14]. In particular, it is necessary to resolve the ground state—which entails averaging for a time $4S_{xx}/x_{zpf}^2$ —before it decoheres, e.g., by heating. The latter happens at a rate $n_{\text{th}}\Gamma_m$, where $n_{\text{th}} = k_B T / \hbar \Omega_m \gg 1$ is the mean occupation of the dominant thermal bath at temperature T . It follows from Eq. (2) that a resolution at the

level of the zero-point-fluctuations is acquired at the measurement rate [9] $\Gamma_{\text{opt}} = 4g^2/\kappa$, where $g = x_{zpf}(\partial\omega_c/\partial x)a$, and $|a|^2$ the number of photons in the cavity (assuming $\eta_c \eta_d = 1$, $\Omega \ll \kappa$). The above-mentioned requirement can then be written as $\Gamma_{\text{opt}} \gtrsim n_{\text{th}}\Gamma_m$.

Interestingly, a completely new effect becomes relevant in this regime as well: the quantum fluctuations of radiation pressure linked to the quantum amplitude fluctuations of the laser light, representing the quantum backaction of this measurement [15]. And indeed the ratio of radiation pressure to thermal Langevin force fluctuations is given by $\frac{S_{FF}^{\text{qba}}(\Omega_m)}{S_{FF}^{\text{th}}(\Omega_m)} = \frac{\Gamma_{\text{opt}}}{n_{\text{th}}\Gamma_m}$. While these force fluctuations induce random mechanical motion that can mask a signal to be measured, it is important to realize that motion and light become correlated, at the quantum level, via this mechanism. As a consequence, the mere interaction of cavity light with a nanomechanical device can induce optical phase–amplitude quantum correlations, which squeeze the optical quantum fluctuations, in a particular quadrature, below the level of the vacuum noise. This effect is referred to as ponderomotive squeezing [16–19].

An example of this phenomenon is shown in Fig. 1c [20]. A 1.928-MHz nanomechanical membrane resonator of dimensions $(544 \mu\text{m})^2 \times 60$ nm is placed in a laser-driven high-finesse optical cavity and thereby measured at a rate of $\Gamma_{\text{opt}}/2\pi = 96$ kHz. Its decoherence rate is reduced to $n\Gamma_m/2\pi \approx 20$ kHz, by cooling it in a simple cryostat to $T = 10$ K. A slight detuning of the laser field with respect to the optical resonator ($\Delta = \omega - \omega_c = -2\pi \times 1.4$ MHz) leads to further cooling of the mechanical mode [21–24], akin to Doppler cooling of atomic gases [25]—here to a mean occupation of $n_{\text{eff}} \sim 5$. It also allows direct observation of the squeezing in the amplitude fluctuations of the light emerging from the resonator: Its normalized spectral density assumes the form

$$S_{XX}^{\text{out}}(\Omega) \approx 1 - 2\frac{8\Delta}{\kappa}\Gamma_{\text{opt}}\text{Re}\{\chi_{\text{eff}}(\Omega)\} + \left(\frac{8\Delta}{\kappa}\right)^2 \Gamma_{\text{opt}}|\chi_{\text{eff}}(\Omega)|^2(\Gamma_{\text{opt}} + n_{\text{th}}\Gamma_m). \quad (3)$$

Note that the second term represents the correlations, which can assume negative values and thus lead to noise below the vacuum level $S_{XX}^{\text{out}} = 1$ (χ_{eff} is the effective mechanical susceptibility [3]). Ponderomotive squeezing down to -2.4 dB has been observed, the strongest value so far, and simultaneous squeezing in a multitude of mechanical modes [20]. Schemes that exploit such quantum correlations for sub-SQL measurements of displacement and forces are subject of ongoing research [26–28].

The above examples show that laser-based measurements resolve the motion of nanomechanical oscillators

all the way to the level of their vacuum fluctuations. In a simple classification (Fig. 1d), basic interferometers can readily resolve thermal motion, as required in many sensing and characterization experiments. Cavity-enhanced approaches achieve imprecision below the resonant SQL. To measure and control motion at the quantum level, displacements at the scale of the vacuum fluctuations must be resolved within the coherence time of the mechanical resonator. Then the imprecision (of an ideal setup) is more than n th times below the resonant SQL, and quantum backaction exceeds thermal force fluctuations and induces quantum correlations [3, 9].

While the above-described techniques can be considered variants of laser interferometry, there are a number of techniques to characterize mechanical devices that are laser spectroscopic in nature. A prominent example is optomechanically induced transparency (OMIT), first described in Refs. [29, 30]. It consists in the observation that a laser-driven cavity containing a dispersively coupled mechanical device will have a modified transmission spectrum for a second “probe” laser beam at the frequency $\omega_p = \omega + \Omega_m + \Delta'$, where $|\Delta'| \lesssim \kappa$ is the two-photon detuning. The intracavity probe field,

$$a_p \propto \frac{\sqrt{\kappa}}{(-i\Delta' + \kappa/2) + \frac{g^2}{-i\Delta' + \Gamma_m/2}} \quad (4)$$

in the simplest case $-\Delta = \Omega_m \ll \kappa$, encodes the coupling strength g . It is thus possible to derive g , for example, from probe transmission measurements [31, 32].

3 Laser-based imaging

As already indicated, it can be of great interest to also spatially resolve mechanical displacement patterns. With laser light, this can be accomplished in an extremely sensitive and virtually non-perturbing manner [33–37]. In the following, we present two methods that we have implemented for characterizing nano- and micromechanical resonators with micrometer transverse resolution, sufficient for resolving the spatial patterns of MHz mechanical modes.

3.1 Scanning laser interferometry

The first setup, shown in Fig. 2, is a Michelson interferometer based on a Nd:YAG laser at $\lambda = 1064$ nm. A polarizing beam splitter (PBS1) splits its output into two interferometer arms. In one arm, a single-mode fiber guides light to a probe head mounted on a motorized 3-axis translation stage. The probe head (Fig. 2a) consists of a microscope objective focusing the laser light to a spot of diameter $\sim 2 \mu\text{m}$ on the sample and a CMOS camera capturing

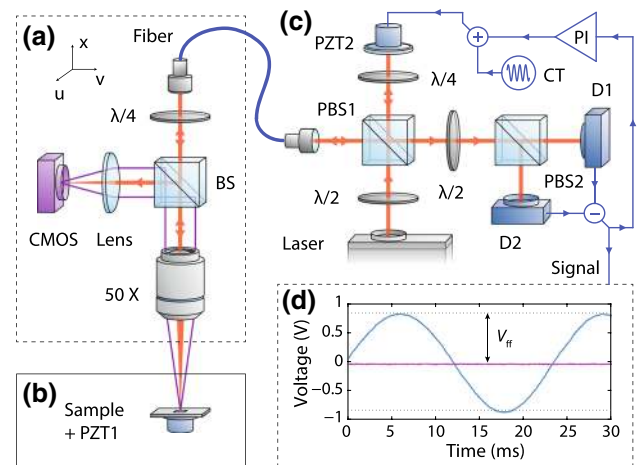


Fig. 2 Setup for interferometric imaging of mechanical motion. **a** Probe head with microscope objective mounted on a motorized 3-axis translation stage to position a focused laser spot on the sample. The sample is imaged simultaneously onto a CMOS camera via a beam splitter (BS) and a lens. **b** Sample placed on top of a piezo (PZT1) inside a high vacuum chamber. **c** Main part of the Michelson interferometer. A balanced receiver (detectors D1 and D2) measures the relative phase between the light returned from the sample and the reference arm. Electronic feedback to a piezomounted mirror (PZT2) stabilizes this phase with a low ($\lesssim 10$ kHz) bandwidth. **d** Signal from the balanced receiver as a function of time while scanning (blue) and actively stabilizing (purple) the relative phase

images of the sample in real time. To reduce viscous (gas) damping of the nanomechanical motion, the sample is placed inside a high vacuum chamber at a pressure of $< 10^{-5}$ mbar. A piezoelectric shaker (PZT1) can excite mechanical eigenmodes (Fig. 2b).

Light reflected off the sample is spatially overlapped with the local oscillator from the other interferometer arm in PBS1 (Fig. 2c). Projection on a common polarization basis subsequently enforces interference in a second polarizing beam splitter (PBS2), whose outputs are monitored with a high-bandwidth (0–75 MHz) InGaAs-balanced receiver. This configuration ensures shot-noise-limited detection of the reflected light when a typical $\sim 800 \mu\text{W}$ beam is sent to the sample. In the correct polarization base, one obtains a receiver signal $V_{\text{ff}} \cos(\phi)$, where ϕ is the relative phase between the two beams and V_{ff} is the full fringe voltage, which we check with an oscilloscope (Fig. 2d). For maximal transduction, ϕ is actively stabilized to the mid-fringe position by means of a mirror mounted on a piezoelectric transducer in the local oscillator arm (PZT2) and a proportional-integral (PI) feedback control.

In this case, small measured voltages $\delta V(t) \ll V_{\text{ff}}$ convert to displacement via $\delta x(t) \approx \pm \delta V(t) \lambda / 4\pi V_{\text{ff}}$. Modulating PZT2 continuously with known frequency and amplitude generates a reference displacement and provides an independent calibration tone (CT) in the spectra.

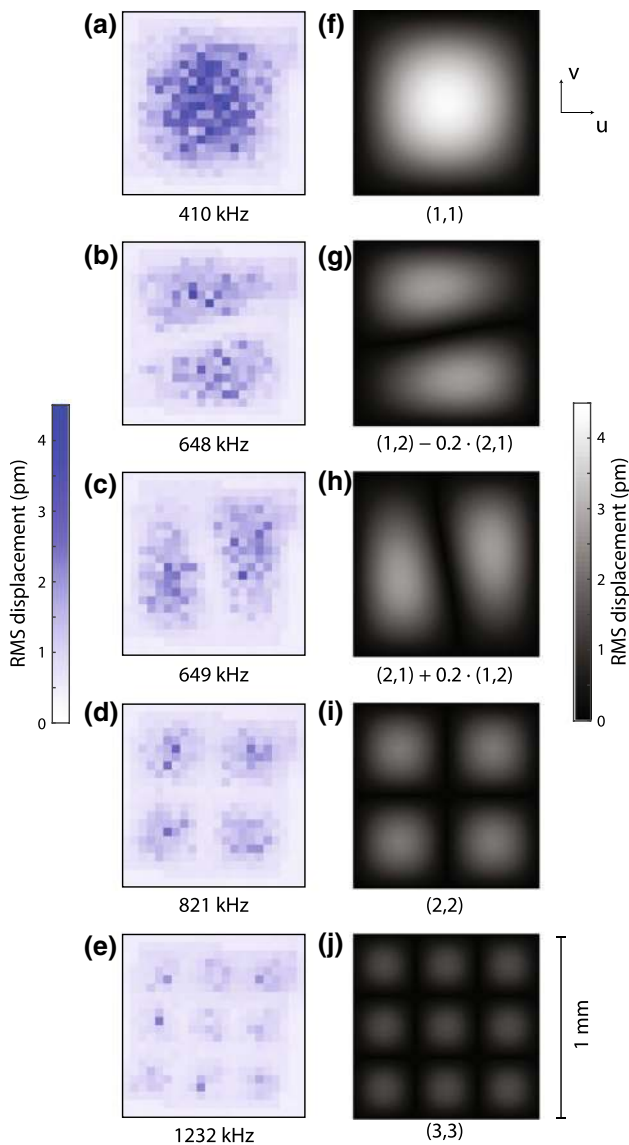


Fig. 3 Nanomechanical modes of a stoichiometric SiN membrane measured with the raster-scan interferometer. **a–e** Measurements of thermal motion on a 22×22 point grid. **f–j** Calculated displacement for mode numbers (n, m) , accounting for hybridization between mode $(1, 2)$ and $(2, 1)$

As a first example, Fig. 3 shows a raster scan of a stoichiometric silicon nitride (SiN) membrane with side length $l = 1$ mm. We scan the membrane surface with the probe head using stepper motor actuation and record traces $\delta x(t)$ at each of the 22×22 positions. The traces are spectrally filtered around the peaks of several mechanical modes via digital post-processing. In this manner, we extract RMS displacements of each mechanical eigenmode in each scan pixel. Figure 3 shows the corresponding displacement maps for the modes, which are thermally excited at room temperature (PZT1 off). The measured mode patterns

compare well with the hybridized eigenmodes of a square membrane:

$$w_{n,m} \propto \sin(k_n u) \sin(k_m v) + \beta \sin(k_m u) \sin(k_n v), \quad (5)$$

where $k_n = 2\pi n/l$, $k_m = 2\pi m/l$, and $n, m \geq 1$ denote the number of antinodes along in-plane coordinates u and v , respectively, and $|\beta| < 1$ quantifies the degree of hybridization between degenerate mode pairs. We find that the measured maximum RMS displacements, as calibrated by the CT, are in good agreement with the expected thermal motion (Fig. 3). Here, we have assumed a mass $m_{\text{eff}} = \rho l^2 h/4 \sim 34$ ng, given the thickness $h = 50$ nm and density $\rho = 2.7$ g/cm³ of the membrane. Note that the modes $(n, m) = (1, 2)$ and $(2, 1)$ show hybridization with $|\beta| \sim 0.2$.

Scanning laser interferometry is particularly useful to characterize complex mode structures, such as SiN membranes patterned with phononic crystal structures [4] (Fig. 4). A scan measured on a grid of 100×100 points with a $5 \mu\text{m}$ spacing resolves also the $9.3 \mu\text{m}$ -wide tethers in between two holes, as Fig. 4b shows. At the expense of measurement time, the grid spacing could be further reduced; however, the spatial resolution of the obtained image is eventually limited to the $\sim 2 \mu\text{m}$ diameter of the laser spot. Figure 4c shows another mode of the same device imaged over a larger area. At a distance of $500 \mu\text{m}$ from the center, the mode's amplitude has decayed to the measurement noise level, illustrating the localization of the mode to the defect.

An advantage of measuring thermally excited modes is that information on all modes within the detector bandwidth is acquired simultaneously. This large set of data can be processed and represented in different ways. As an example, Fig. 4c shows an average spectrum of 400 measurement points on the defect. It clearly reveals a phononic bandgap between about 1.41 and 1.68 MHz, containing five defect mode peaks, as well as the calibration peak at 1.52 MHz. The left panel shows a displacement map corresponding to a specific frequency bin of this spectrum. We can also create an animation that composes the displacement maps for each of the frequency bins in the spectrum. It is provided as electronic supplementary material to this article (see supplementary material). It delivers an instructive illustration of the effect of the phononic crystal structure, contrasting the small number of localized modes inside the bandgap with a “forest” of distributed modes at frequencies outside the bandgap.

A disadvantage of the scanning laser interferometer is its long measurement time. For instance, a high-resolution scan, such as the one shown in Fig. 4b, takes more than 8 hours. This is because for each pixel of the image we probe thermal motion during several seconds, averaging over

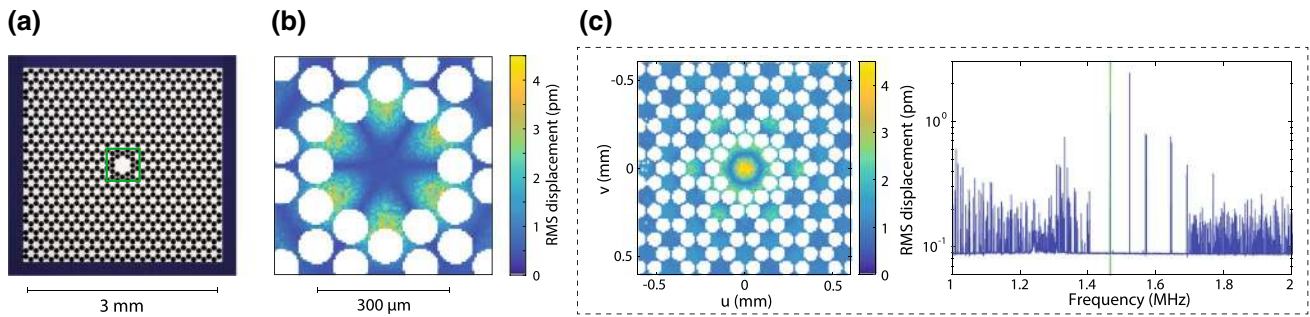


Fig. 4 Measurements of patterned SiN membrane with the raster-scan interferometer. **a** Micrograph of a SiN membrane patterned with a phononic crystal structure. **b** Localized nanomechanical mode imaged on 100×100 grid in the scan area indicated by a green square in **(a)**. Holes are detected by disappearance of the calibration peak

and shown as white pixels. **c** Snapshot of an animation provided as supplementary material. It shows the displacement pattern (left) corresponding to a particular frequency bin (green line) of the averaged spectrum (right) (from [4])

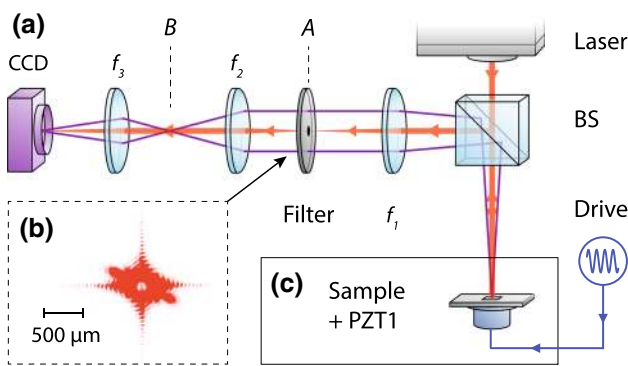


Fig. 5 Setup for dark-field imaging of mechanical motion. **a** Optical configuration with small opaque disk in the Fourier plane *A*, creating a dark-field image of the sample in the image plane *B*. A lens (f_3) projects a magnified image onto a CCD camera. A ray diagram illustrates how the image is formed (purple lines). **b** Image of the Fourier plane, where an opaque disk blanks out undiffracted zero-order light, when a membrane mode is excited. **c** Sample is mounted on a piezoelectric actuator (PZT1) in a high vacuum chamber

timescales longer than Γ_m^{-1} . Some acceleration is possible by either artificially increasing Γ_m , e.g., by controlled gas damping, or by driving the modes coherently using PZT1. The latter can furthermore provide information about the mechanical phase at each position, if mechanical frequency drifts are properly accounted for.

3.2 Dark-field imaging

A powerful approach to single-shot characterization of mechanical modes is provided by dark-field imaging [35]. Figure 5a shows the setup which we have implemented to this end. It directly captures the squared displacement patterns of two-dimensional resonators such as membranes or cantilevers on a CCD camera. Its functional principle is described with simple Fourier optics [38]. A collimated

laser beam with a wavelength $\lambda = 1064 \text{ nm}$ and beam diameter of 2.4 mm impinges perpendicularly on the sample, here a SiN membrane with side length $l = 1 \text{ mm}$. The reflected electric field E_r at transverse position (u, v) is subject to a phase shift proportional to the membrane displacement $w(u, v, t)$. We assume that the incident electric field $E_0 e^{i\omega t}$ is constant across the membrane, since the incident beam diameter is 2.4 times larger than the membrane. Assuming furthermore $w(u, v, t) \ll \lambda$, the reflected electric field reads $E_r(u, v, t) \approx r E_0 e^{i\omega t} [1 + ikw(u, v, t)]$, where r is the absolute value of the reflection coefficient, $k = 2\pi/\lambda$ and $\omega = ck$. A lens (focal length $f_1 = 75 \text{ mm}$) performs an optical Fourier transform \mathcal{F} with respect to the coordinates (u, v) , yielding

$$\mathcal{F}(E_r) = r E_0 e^{i\omega t} [\mathcal{F}(1) + \mathcal{F}(ikw(u, v, t))]. \tag{6}$$

The zero-order peak (first term in Eq. (6)) is removed from the beam by an opaque disk in the Fourier plane. This extracts the diffracted light due to the membrane displacement w . A second, subsequent lens (focal length $f_2 = 50 \text{ mm}$) performs another Fourier transform on the filtered light. The time-averaged intensity pattern

$$\begin{aligned} I(u', v') &= \left\langle \left| r E_0 e^{i\omega t} \mathcal{F}(\mathcal{F}(ikw(u, v, t))) \right|^2 \right\rangle \\ &= I_0 r^2 k^2 \left\langle w(-u, -v, t)^2 \right\rangle, \end{aligned} \tag{7}$$

is then recorded by a camera, where $I_0 = |E_0 e^{i\omega t}|^2$ is the incident intensity. It directly shows an intensity pattern proportional to the squared displacement of an eigenmode.

In our setup, a third lens with focal length $f_3 = 35 \text{ mm}$ is placed in front of the camera to magnify the image. It also allows imaging the Fourier plane by adjusting the distance between camera and lens to f_3 . Figure 5b shows a Fourier image of the membrane with diffraction patterns extending in two orthogonal directions due to the sharp edges of the

membrane. Two bright spots close to the center originate from diffraction due to a driven eigenmode, a hybridization between the modes (1,2) and (2,1) at a frequency of 645 kHz. The opaque disk made of aluminum deposited on a thin piece of glass is seen as a white disk in the center. With a diameter $d = 100 \mu\text{m}$, it blocks diffraction angles $\alpha \lesssim d/2f_1$ generated by mechanical modes with a distance between nodes of $\gtrsim \lambda/2\alpha \approx 800 \mu\text{m}$.

A piezoelectric actuator (PZT1) successively excites the eigenmodes of the SiN membrane inside a vacuum chamber, by slowly sweeping a strong drive tone across the frequency window of interest (here 0.4...2 MHz). Figure 6 shows images of several modes recorded with an incident optical power of $\sim 100 \mu\text{W}$ and a typical integration time of 10 ms. Comparison with mode patterns calculated from Eq. (5) allows inferring the mode numbers (n, m), and the degree of hybridization, as seen, for example, on the 1.683-MHz mode.

While it enables much shorter measurement times than the scanning laser interferometer, the dark-field imaging setup has a relatively low displacement sensitivity. For this reason, PZT1 has to be driven with a stroke of $\gtrsim 300 \text{ pm}$, significantly increasing the membrane oscillation amplitude, up to a regime where mechanical nonlinearities (e.g., Duffing-type frequency shifts) can play a role. In principle, the sensitivity can be enhanced by increasing the laser intensity I_0 , yet in practice it is often limited by background noise due to scattered light from optical components increasing equally with I_0 . Another important limitation is that diffraction from the sample's geometry cannot be discriminated from modal displacements. In this simple implementation, the approach is thus unsuitable for devices with fine structures in their geometry, such as the patterned membranes.

4 Conclusion

In summary, we have described several laser-based techniques to measure and image nanomechanical motion. As we show, exquisite displacement sensitivity can be reached, well into the regime in which quantum backaction and the ensuing light-motion quantum correlations dominate over thermomechanical noise. This sensitivity is rivaled only by techniques based on superconducting microwave electro-mechanical systems, which operate at ultra-low ($T \ll 1 \text{ K}$) cryogenic temperatures [39, 40]. Interest in this quantum domain has originally been motivated by observatories such as LIGO and can now, for the first time, be explored with optical and microwave experiments [3, 9, 15, 41, 42]. In addition, laser-based techniques can provide spatial imaging of mechanical displacement patterns. They constitute not only highly useful tools to develop and characterize

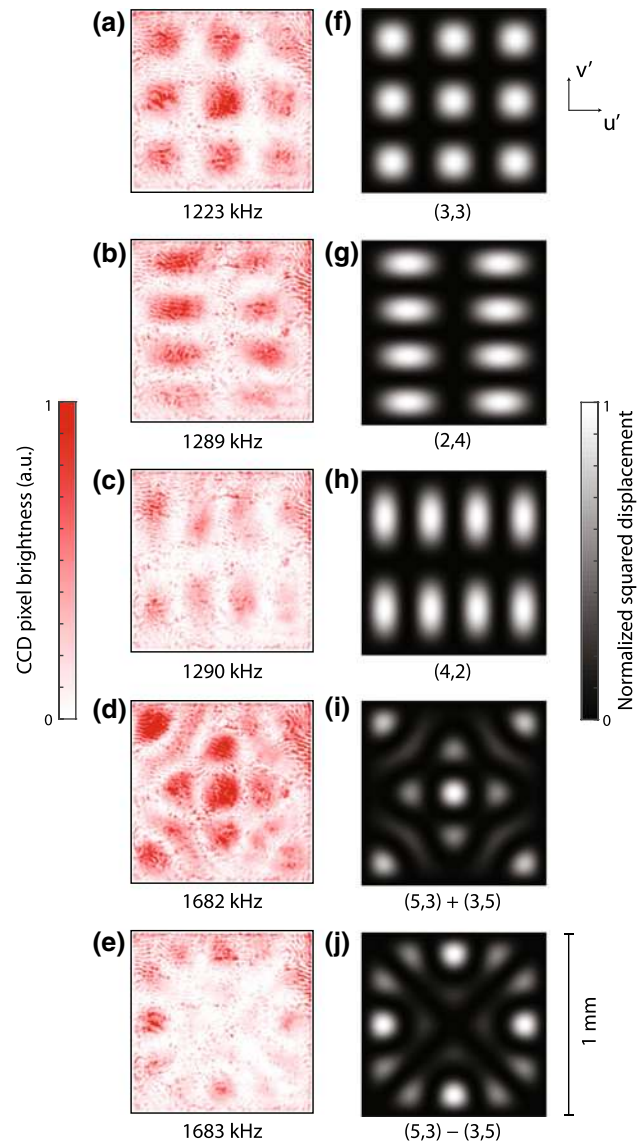


Fig. 6 Nanomechanical modes of a stoichiometric SiN membrane measured with dark-field imaging. **a–e** Single-shot (acquisition time $\sim 10 \text{ ms}$) measurements of mechanical modes at various frequencies while driving the membrane with PZT1. *Pixels colored in dark red indicate high intensities and correspond to large values of squared mechanical displacement.* **f–j** Calculated squared mechanical mode patterns with mode numbers (n, m). Modes (3, 5) and (5, 3) show nearly complete hybridization with $|\beta| \sim 1$

novel micro- and nanomechanical devices [4, 6, 35–37]. Similar techniques could also be used to address individual elements in multimode devices [20] or (opto-)mechanical arrays [4, 43]—if need be, also in combination with cavity-enhanced readout [33, 44].

Acknowledgements We would like to acknowledge our (former and present) colleagues Georg Anetsberger, Olivier Arcizet, Tobias Kippenberg, Jörg H. Müller, Eugene S. Polzik, Andreas Næsby Rasmussen, Remi Rivière, Anders Simonsen, Koji Usami, Stefan Weis, and

Dalziel J. Wilson for their contributions to the work discussed here. Financial support came from the ERC starting grant Q-CEOM, a starting grant from the Danish Council for Independent Research, the EU FP7 grant iQUOEMS, and the Carlsberg Foundation.

References

- B.P. Abbott, R. Abbott, T.D. Abbott, M.R. Abernathy, F. Acernese, K. Ackley, C. Adams, T. Adams, P. Addesso, R.X. Adhikari et al., *Phys. Rev. Lett.* **116**, 061102 (2016)
- D. Rugar, R. Budakian, H.J. Mamin, B.W. Chui, *Nature* **430**, 329 (2004)
- M. Aspelmeyer, T.J. Kippenberg, F. Marquardt, *Rev. Mod. Phys.* **86**, 1391 (2014)
- Y. Tsaturyan, A. Barg, E.S. Polzik, A. Schliesser, [arXiv:1608.00937](https://arxiv.org/abs/1608.00937) (2016)
- J.W. Wagner, J.B. Spicer, *J. Opt. Soc. Am. B* **4**, 1316 (1987)
- Y. Tsaturyan, A. Barg, A. Simonsen, L.G. Villanueva, S. Schmid, A. Schliesser, E.S. Polzik, *Opt. Express* **6**, 6810 (2013)
- A. Schliesser, G. Anetsberger, R. Rivière, O. Arcizet, T.J. Kippenberg, *New J. Phys.* **10**, 095015 (2008)
- T.W. Hänsch, B. Couillaud, *Opt. Commun.* **35**, 441 (1980)
- A.A. Clerk, M.H. Devoret, S.M. Girvin, F. Marquardt, R.J. Schoelkopf, *Rev. Mod. Phys.* **82**, 1155 (2010)
- A. Schliesser, T. J. Kippenberg, Cavity optomechanics with whispering-gallery modeoptical micro-resonators. in *Advances in Atomic, Molecular and Optical Physics*, vol. 58, Chap. 5, ed. by P. Berman, E. Arimondo, C. Lin (Elsevier Academic Press, 2010), pp. 207–323
- S. Stapfner, L. Ost, D. Hunger, J. Reichel, I. Favero, E.M. Weig, *Appl. Phys. Lett.* **102**, 151910 (2013)
- G. Anetsberger, O. Arcizet, Q.P. Unterreithmeier, R. Rivière, A. Schliesser, E.M. Weig, J.P. Kotthaus, T.J. Kippenberg, *Nat. Phys.* **5**, 909 (2009)
- G. Anetsberger, E. Gavartin, O. Arcizet, Q.P. Unterreithmeier, E.M. Weig, M.L. Gorodetsky, J.P. Kotthaus, T.J. Kippenberg, *Phys. Rev. A* **82**, 061804 (2010)
- D.J. Wilson, V. Sudhir, N. Piro, R. Schilling, A. Ghadimi, T.J. Kippenberg, *Nature* **524**, 325 (2015)
- C.M. Caves, *Phys. Rev. Lett.* **45**, 75 (1980)
- C. Fabre, M. Pinard, S. Bourzeix, A. Heidmann, E. Giacobino, S. Reynaud, *Phys. Rev. A* **49**, 1337 (1994)
- S. Mancini, P. Tombesi, *Phys. Rev. A* **49**, 4055 (1994)
- T.P. Purdy, P.-L. Yu, R.W. Peterson, N.S. Kampel, C.A. Regal, *Phys. Rev. X* **3**, 031012 (2013)
- A.H. Safavi-Naeini, S. Gröblacher, J.T. Hill, J. Chan, M. Aspelmeyer, O. Painter, *Nature* **500**, 185 (2013)
- W.H.P. Nielsen, Y. Tsaturyan, C.B. Møller, E.S. Polzik, A. Schliesser, [arXiv:1605.06541](https://arxiv.org/abs/1605.06541) (2016)
- O. Arcizet, P.-F. Cohadon, T. Briant, M. Pinard, A. Heidmann, *Nature* **444**, 71 (2006)
- S. Gigan, H.R. Böhm, M. Paternosto, F. Blaser, G. Langer, J.B. Hertzberg, K.C. Schwab, D. Bäuerle, M. Aspelmeyer, A. Zeilinger, *Nature* **444**, 67 (2006)
- A. Schliesser, P. Del’Haye, N. Nooshi, K. Vahala, T. Kippenberg, *Phys. Rev. Lett.* **97**, 243905 (2006)
- J.D. Thompson, B.M. Zwickl, A.M. Jayich, F. Marquardt, S.M. Girvin, J.G.E. Harris, *Nature* **452**, 72 (2008)
- T.W. Hänsch, A.L. Schawlow, *Opt. Commun.* **13**, 68 (1975)
- O. Arcizet, T. Briant, A. Heidmann, M. Pinard, *Phys. Rev. A* **73**, 033819 (2006)
- L.F. Buchmann, S. Schreppler, J. Kohler, N. Spethmann, D.M. Stamper-Kurn, *Phys. Rev. Lett.* **117**, 030801 (2016)
- N.S. Kampel, R.W. Peterson, R. Fischer, P.-L. Yu, K. Cicak, R.W. Simmonds, K.W. Lehnert, C.A. Regal, [arXiv:1607.06831](https://arxiv.org/abs/1607.06831) (2016)
- A. Schliesser, Cavity optomechanics and optical frequency comb generation with silica whispering-gallery-mode microresonators, Ph.D. thesis, Ludwig-Maximilians-Universität München, 2009
- G.S. Agarwal, S. Huang, *Phys. Rev. A* **81**, 041803 (2010)
- S. Weis, R. Rivière, S. Deléglise, E. Gavartin, O. Arcizet, A. Schliesser, T.J. Kippenberg, *Science* **330**, 1520 (2010)
- A.H. Safavi-Naeini, T.P. Mayer, I. Alegre, J. Chan, M. Eichenfield, M. Winger, J.Q. Lin, J.T. Hill, D.E. Chang, O. Painter, *Nature* **472**, 69 (2011)
- T. Briant, P.-F. Cohadon, A. Heidmann, M. Pinard, *Phys. Rev. A* **68**, 033823 (2003)
- O. Arcizet, P.-F. Cohadon, T. Briant, M. Pinard, A. Heidmann, J.-M. Mackowski, C. Michel, L. Pinard, O. Francais, L. Rousseau, *Phys. Rev. Lett.* **97**, 133601 (2006)
- S. Chakram, Y.S. Patil, L. Chang, M. Vengalattore, *Phys. Rev. Lett.* **112**, 127201 (2014)
- Z. Wang, J. Lee, P.X.L. Feng, *Nat. Commun.* **5**, 5158 (2014)
- D. Davidovikj, J.J. Slim, S.J. Cartamil-Bueno, H.S.J. van der Zant, P.G. Steeneken, W.J. Venstra, *Nano Lett.* **16**, 2768 (2016)
- See Supplementary Material
- W. Lauterborn, T. Kurz, M. Wiesenfeldt, *Coherent Optics* (Springer, Berlin, 1995)
- J.D. Teufel, R. Donner, M.A. Castellanos-Beltran, J.W. Harlow, K.W. Lehnert, *Nat. Nanotech.* **4**, 820 (2009)
- J.D. Teufel, F. Lecocq, R.W. Simmonds, *Phys. Rev. Lett.* **116**, 013602 (2016)
- V.B. Braginsky, F.Y. Khalili, *Quantum Measurement* (Cambridge University Press, Cambridge, 1992)
- I. Tittonen, G. Breitenbach, T. Kalkbrenner, T. Müller, R. Conradt, S. Schiller, E. Steinsland, N. Blanc, N.F. de Rooij, *Phys. Rev. A* **59**, 1038–1044 (1999)
- G. Heinrich, M. Ludwig, J. Qian, B. Kubala, F. Marquardt, *Phys. Rev. Lett.* **107**, 043603 (2011)
- M. Mader, J. Reichel, T.W. Hänsch, D. Hunger, *Nat. Commun.* **6**, 7249 (2015)